Supporting Information for

Solutal and Thermal Buoyancy Effects in Self-Powered Phosphatase Micropumps

Lyanne Valdez,[†1] Henry Shum,[§1] Isamar Ortiz-Rivera,[†] Anna C. Balazs,[§*] and Ayusman Sen[†*]

[†]Department of Chemistry, The Pennsylvania State University, University Park, PA 16802

[§]Department of Chemical & Petroleum Engineering, University of Pittsburgh, Pittsburgh, PA 15261

[1.] These authors contributed equally to the work.

*Email: balazs@pitt.edu, asen@psu.edu

Supplementary Methods and Materials

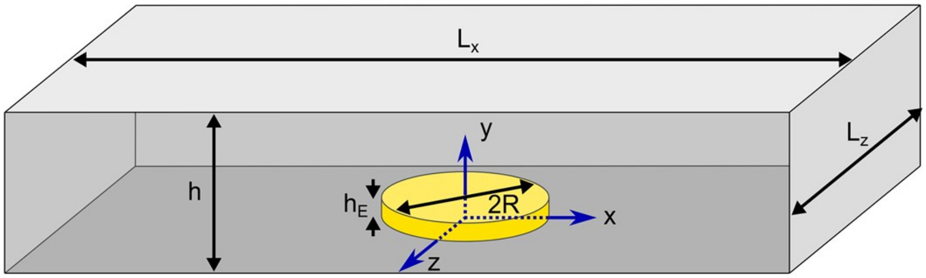

Figure S1. Geometry used in the theoretical model. The enzyme patch (thin disc) pumps fluid within an enclosed chamber of height h = 0.9 mm and horizontal lengths $L_x = L_z$ = 20 mm.

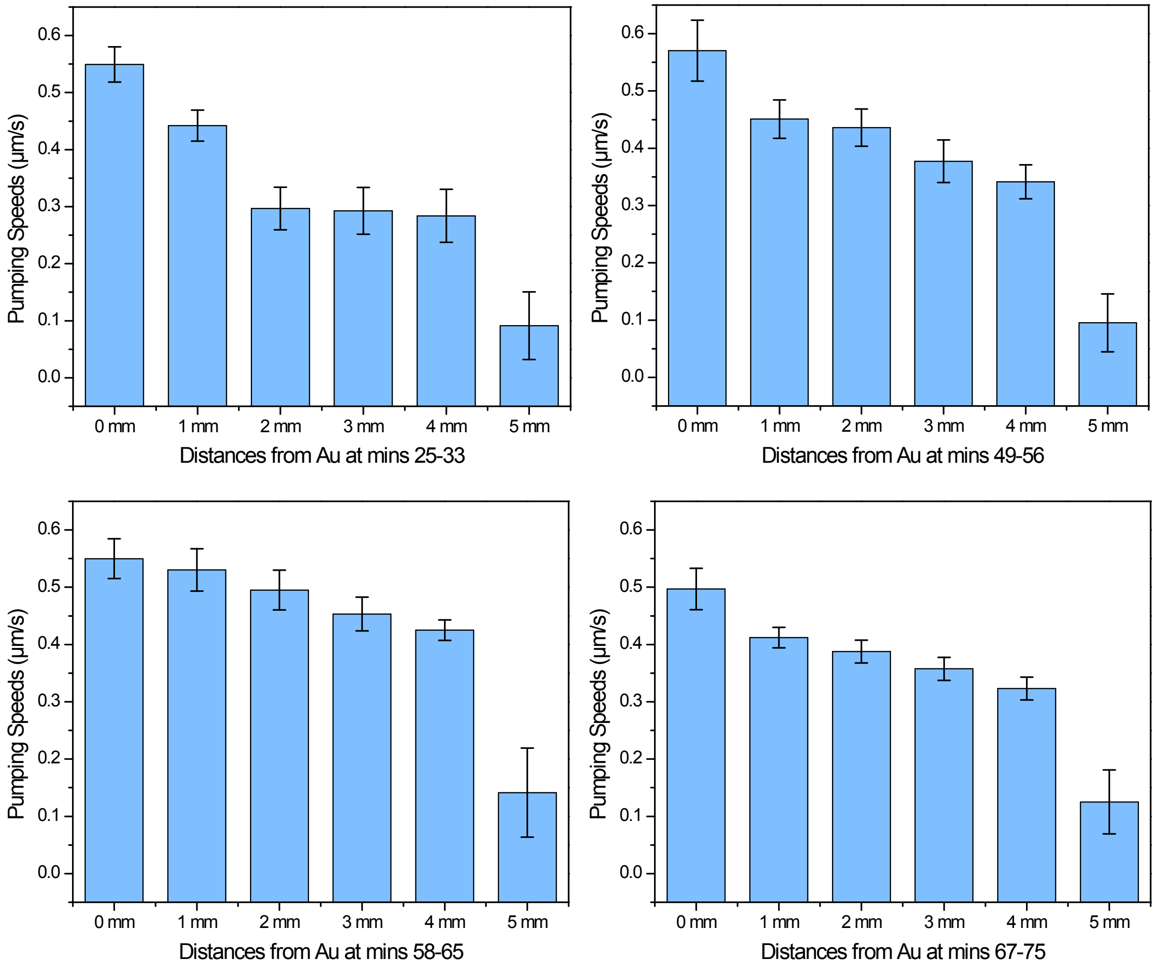

Figure S2. Pumping behavior of acid phosphatase micropumps as a function of distance and time in the presence of 50 mM pNPP. The progression of the fluid flow at different distances away from the Au patch is shown over the course of different time periods, where 0 mm is at the edge of the Au patch and 5 mm is approaching the wall of the chamber. With time, the fluid flow begins to spread from the edge of the Au patch to the wall and then begins to diminish after some time (approximately 1 hr).

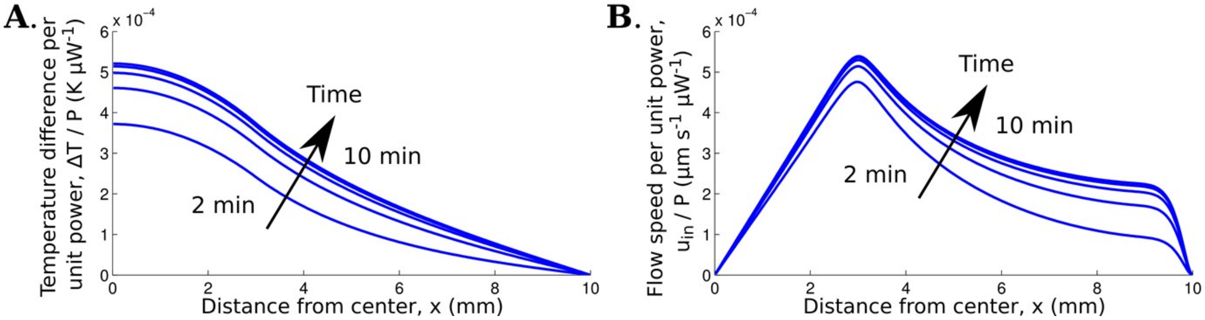

Figure S3. Simulated spatial and temporal variations in temperature and pumping speeds driven by thermal buoyancy effects. Curves are plotted at time intervals of 2 min. The perimeter of the pump lies at $x = 3$ mm. (A) Vertically averaged temperature differences relative to initial temperature, normalized by the pump heat generation power, P. (B) Pumping speeds normalized by pump power, P. The inward flow speed u_{in} is defined as the horizontal flow speed in the direction toward the center of the pump at the height $y = 50$ μm.

Control Experiments

The pumping behavior was studied without the immobilization of acid phosphatase and observed in the presence of 50 mM pNPP. No directional pumping was observed and only Brownian diffusion of the tracer particles resulted, and is represented by the pumping speeds values below 0.1 μm/s. The behavior of the pump with and without acid phosphatase in 50 mM pNPP is shown in Figure S4. Similar studies were performed with the acid phosphatase pumps in the presence of 0 mM pNPP. No directional pumping was observed, only Brownian diffusion occurred. The behavior of the acid phosphatase pumps in 50 mM and 0 mM pNPP is shown in Figure S5.

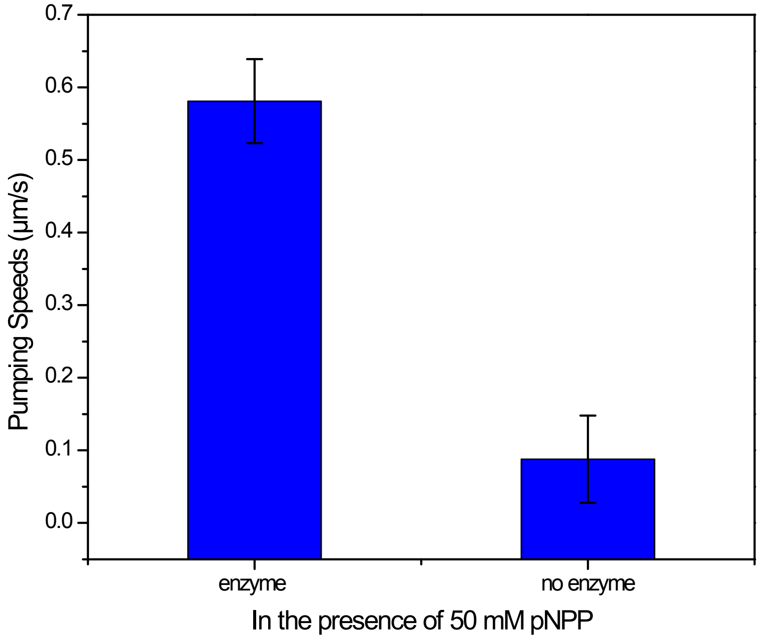

Figure S4. Pumping speeds with and without acid phosphatase in the presence of 50 mM pNPP.

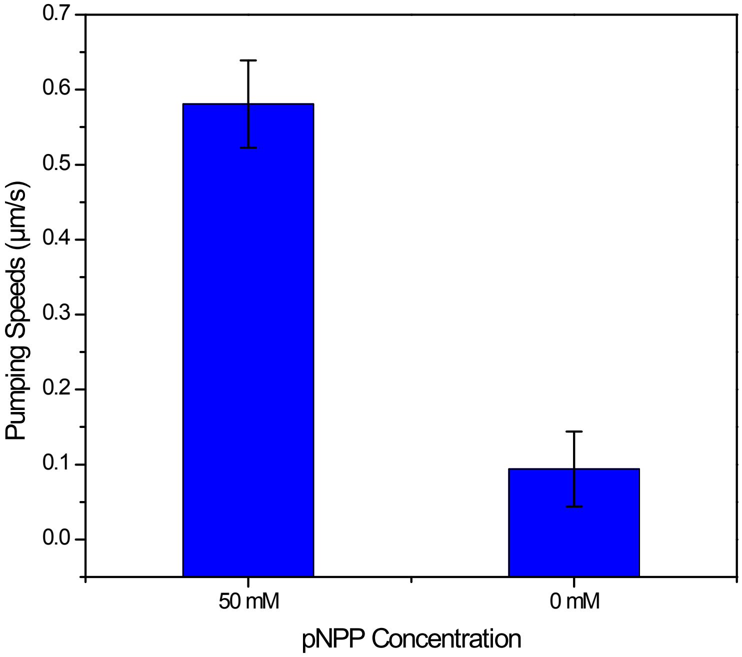

Figure S5. Pumping speeds of the acid phosphatase micropump in the presence of 50 mM and 0 mM pNPP.

Numerical Methods

The geometry used in the theoretical model is illustrated in Figure S1. The interior of the chamber is described by the conditions $|x| < L_x/2$, $0 < y < h$, and $|z| < L_z/2$. We verified by preliminary simulations that, as expected from the symmetry of the setup, the temperature, concentration and flow fields all satisfied reflectional symmetry in the $x = 0$ and $z = 0$ planes. This allowed us to increase the spatial resolution of the simulation, maintaining an equivalent computational load, by solving the governing equations restricted to the subdomain $0 < x < L_x/2,\ 0 < y < h,\ 0 < z < L_z/2$. Boundary conditions imposed on the symmetry planes $x = 0$ and $z = 0$ were no heat and chemical flux, and free fluid slip, expressed mathematically as

$$\left.\frac{\partial T}{\partial z}\right|_{x=0} = \left.\frac{\partial T}{\partial x}\right|_{z=0} = 0,$$

$$\left.\frac{\partial c}{\partial z}\right|_{x=0} = \left.\frac{\partial c}{\partial x}\right|_{z=0} = 0,$$

$$\left.u_x\right|_{x=0} = \left.\frac{\partial u_y}{\partial x}\right|_{x=0} = \left.\frac{\partial u_z}{\partial x}\right|_{x=0} = 0,\quad \left.\frac{\partial u_x}{\partial z}\right|_{z=0} = \left.\frac{\partial u_y}{\partial z}\right|_{z=0} = \left.u_z\right|_{z=0} = 0,$$

where u_x, u_y, and u_z are the *x*-, *y*-, and *z*-components of the fluid velocity respectively. The computation grid size was $300 \times 27 \times 300$ with grid spacing $\Delta x = 33.3\,\mu\text{m}$.

Temperature and concentration fields were simulated using the finite difference approach with the forward-time central-space (FTCS) scheme for diffusion.[S1] In the case of concentration fields, advective transport was included using the first order upwind scheme. The time step size in thermal simulations was $\Delta t = 250\,\mu\mathrm{s}$ and the thermal diffusivity was set to $\alpha = 1.43\times10^{-7}\,\mathrm{m^2s^{-1}}$. Simulations of solute transport assumed a diffusion coefficient $D = 10^{-9}\,\mathrm{m^2s^{-1}}$ and were performed with a time step size $\Delta t = 9.26\,\mathrm{ms}$.

A lattice Boltzmann method was used to solve the equations of fluid flow, Eq. 3.[S2] We implemented the single-relaxation-time, D3Q19 model with the standard bounce-back rule to enforce no-slip fluid flow conditions on the chamber walls and specular reflection on the free-slip boundaries.[S3] Flow fields due to thermal effects were obtained by computing the buoyancy force field from the finite difference solutions for the temperature field and executing the lattice Boltzmann algorithm for 5000 time steps until the flow field became steady. The time step size $\Delta t = 185\,\mu\mathrm{s}$ and lattice Boltzmann relaxation parameter $\omega = 1$ were used to achieve the kinematic viscosity $\nu = (1/6)\Delta x^2/\Delta t = 10^{-6}\,\mathrm{m^2s^{-1}}$. For solutal buoyancy simulations, the lattice Boltzmann algorithm was performed in parallel with the finite difference method to couple the fluid advection and buoyancy force field with the solute transport. Hybrid lattice Boltzmann-finite difference schemes have been employed previously for advection-diffusion problems.[S4,S5]

Simulations of Thermal Buoyancy Effects with Different Boundary Conditions

We considered three sets of boundary conditions for the temperature field and compared the results to assess the influence of thermal boundary conditions on the pumping speeds. The three cases of boundary conditions were

(I) no heat flux through all walls;
(II) no heat flux through top and bottom walls, fixed temperature $T = T_0$ on side walls; and
(III) no heat flux through bottom wall, fixed temperature $T = T_0$ on top and side walls.

These three sets of thermal boundary conditions represent idealizations of possible chamber constructions. In typical experimental setups, the chamber walls are not perfect insulators or perfect heat absorbers but lie somewhere in between, allowing heat to escape but also allowing variations in temperature. A fourth candidate for boundary conditions, fixed temperature on all walls, was not considered. Since heat is produced in a thin patch on the bottom wall, constraining the temperature of this wall would immediately remove the generated heat and there would be negligible temperature variations in the chamber.

The vertically averaged temperature changes (relative to the initial temperature) at different distances from the pump are plotted for the three boundary conditions in Figures S6-S8, respectively. Since heat cannot leave the system with boundary conditions I, the temperature rises indefinitely but the temperature gradient stabilizes within 10 min (Figure S6). With boundary conditions II, heat escapes through the side walls and results in a steady temperature profile after 10 min (Figure S7). With boundary conditions III, heat is lost more quickly through the top and side walls, resulting in a steady temperature field within 2 min (Figure S8).

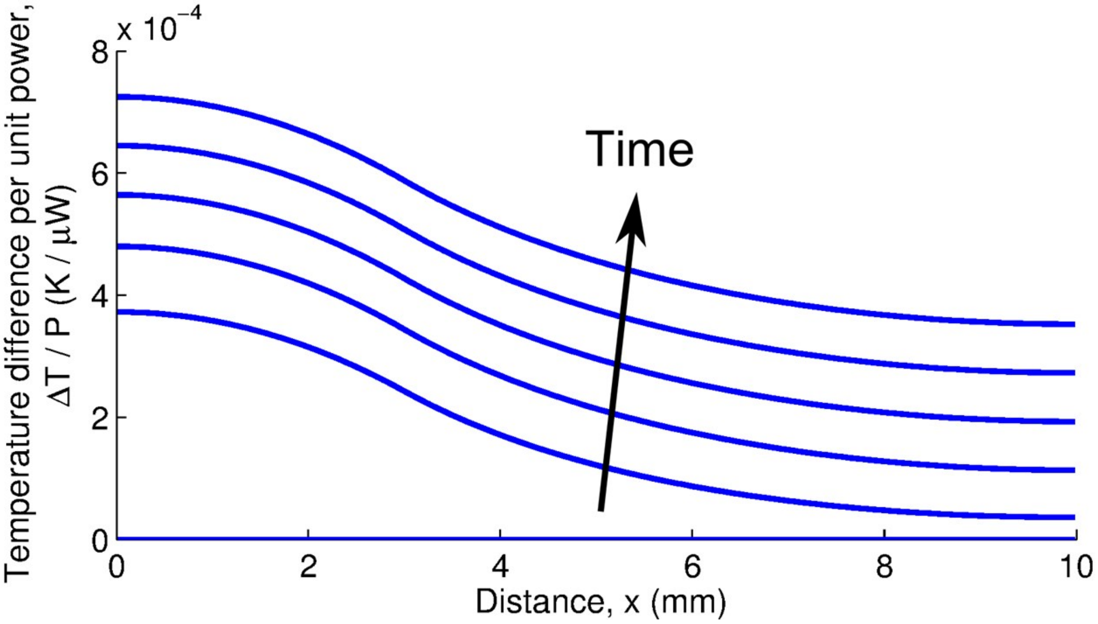

Figure S6. Vertically averaged temperatures in simulations as time increases using boundary condition I. Curves are plotted at 2 min intervals from 0 to 10 min. Since heat cannot escape, the temperature rises gradually with time but the temperature gradient stabilizes.

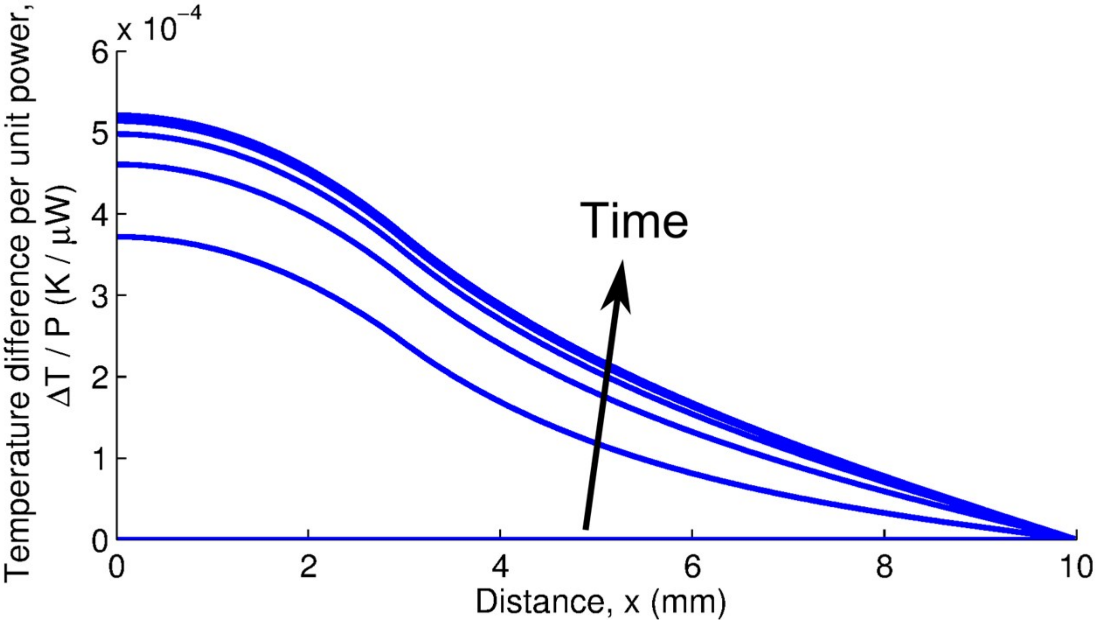

Figure S7. Vertically averaged temperatures in simulations as time increases using boundary condition II. Curves are plotted at 2 min intervals from 0 to 10 min. A steady temperature field is reached after ~10 min.

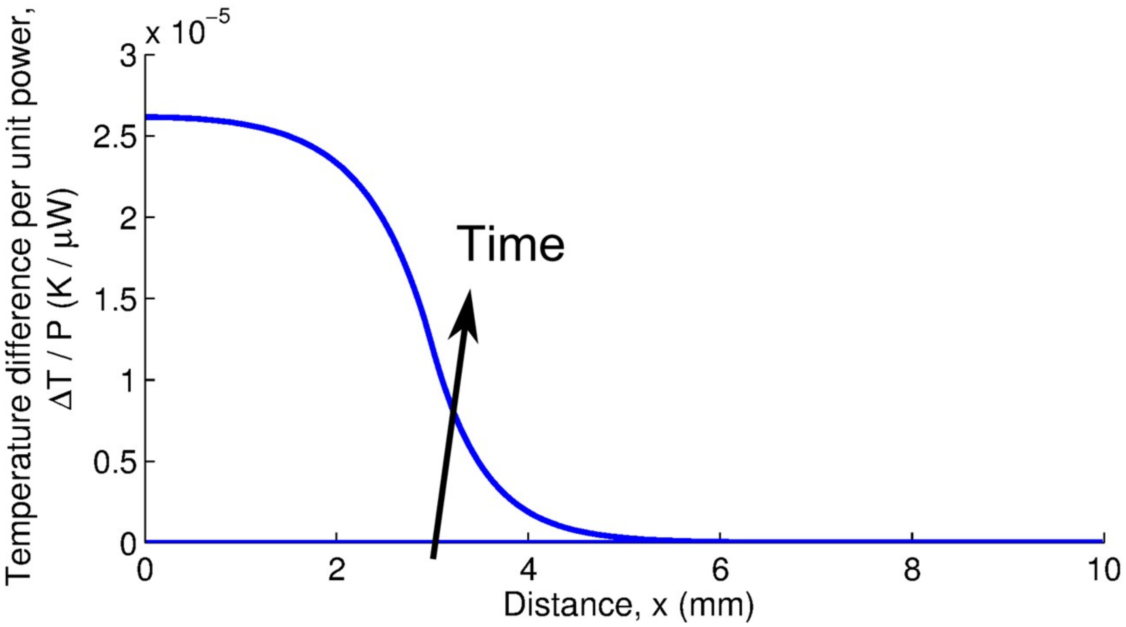

Figure S8. Vertically averaged temperatures in simulations as time increases using boundary condition III. Curves are plotted at 2 min intervals from 0 to 10 min. A steady temperature field is reached in the first 2 min.

The temperature fields in the vertical cross section through the pump for the three sets of boundary conditions are shown in Figure S9. The corresponding flow fields are shown in Figure S10. For comparison with experimental results, we plot the flow speeds at the fixed observation height $y = 50\,\mu\text{m}$ for the three boundary conditions in Figure S11A. We also plot the vertically averaged temperature changes at different distances from the pump center (Figure S11B). The speeds and temperature changes are normalized by the heat generation power, *P*.

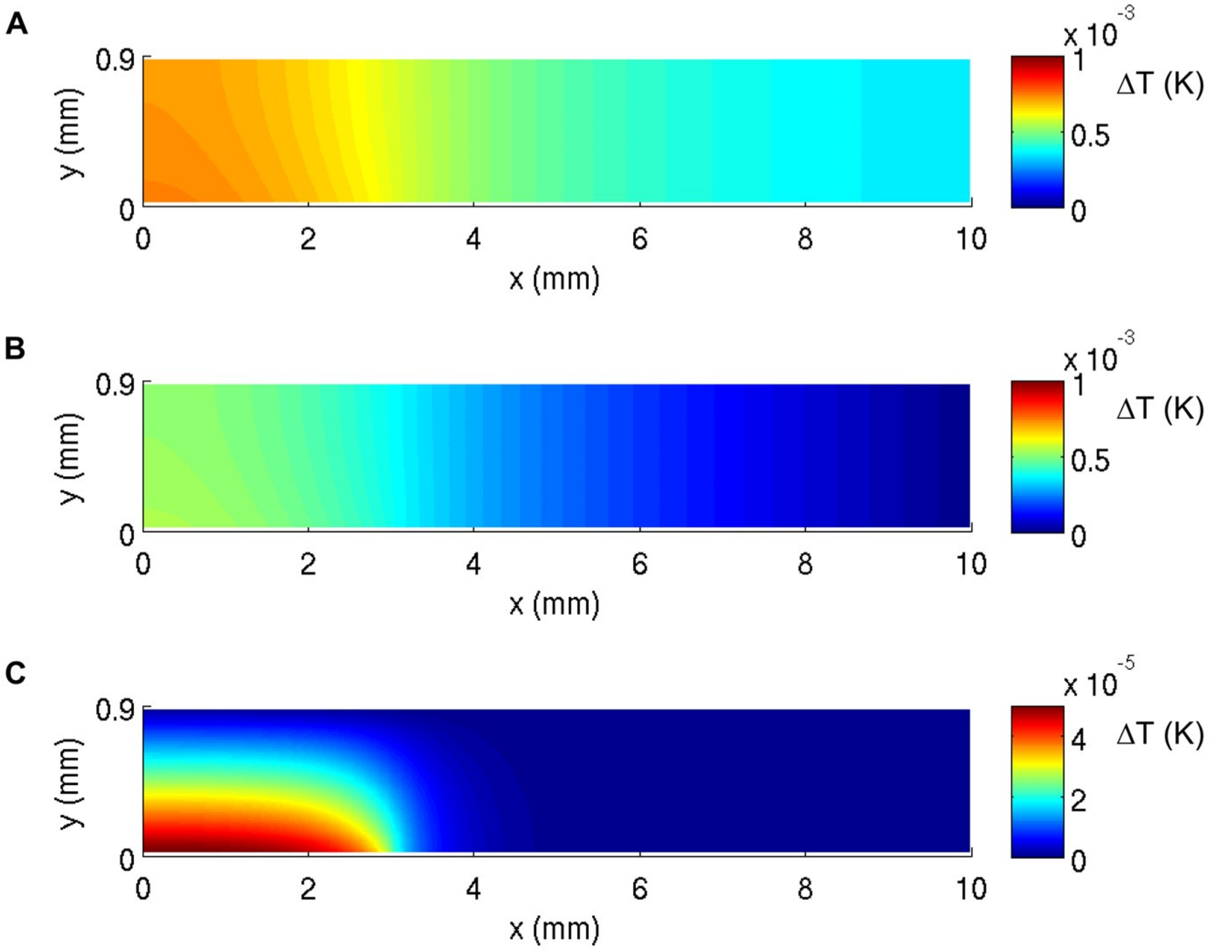

Figure S9. Side views of simulated temperature fields at time t = 10 min using boundary conditions (A) I, (B) II, and (C) III. The color map indicates temperature change ΔT relative to the initial temperature using a fixed heat production rate P = 1 μW.

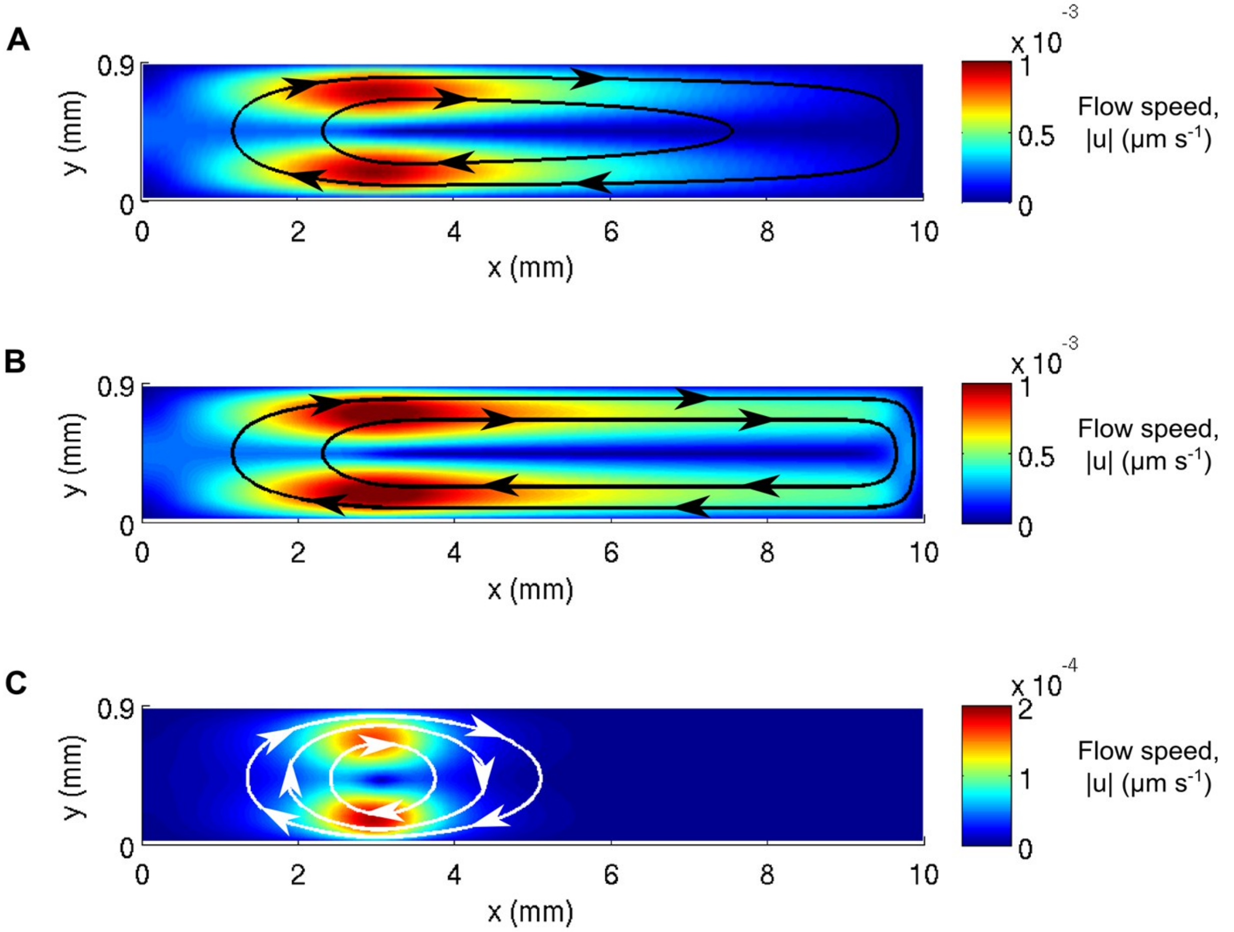

Figure S10. Side views of simulated fluid flow speeds and streamlines at time *t* = 10 min using boundary conditions (A) I, (B) II, and (C) III. The color map indicates the local magnitude of flow using a fixed heat production rate *P* = 1 μW.

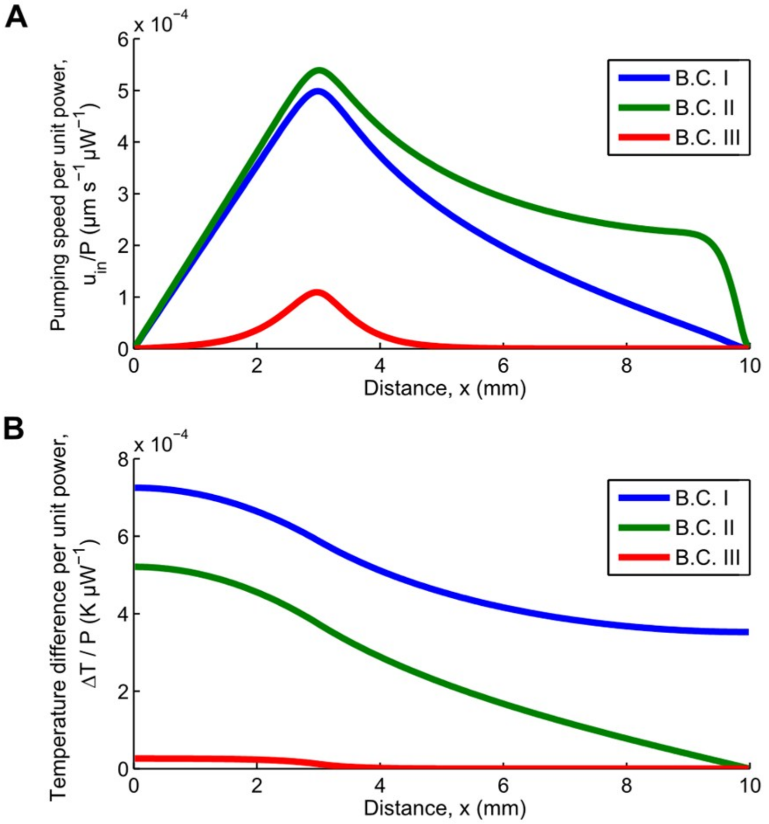

Figure S11. Variations in simulated pumping speeds and temperatures with horizontal distance at time *t* = 10 min. The perimeter of the pump lies at *x* = 3 mm. (A) Pumping speeds, defined as the horizontal flow speeds in the inward (toward the center) direction at the height *y* = 50 μm, normalized by the rate of heat generation. (B) Vertically averaged temperature differences (relative to initial temperature) normalized by the rate of heat generation.

Cases I and II produced similar flow speeds close to the pump. This result is reasonable since the boundary conditions differ only on the side walls, far from the pump. The pumping speed increased linearly with x from zero up to a maximum flow speed per unit power $u_{\max} \approx 5\times10^{-4}\ \mu\mathrm{m\,s^{-1}}\ \mu\mathrm{W}^{-1}$ at the perimeter of the pump ($x = 3\,\mathrm{mm}$) for both cases. The flow speed gradually decreased with distance beyond the pump and, as required by the no-slip boundary conditions, there was no fluid flow at the side walls ($x = 10\,\mathrm{mm}$). The flow speeds far from the pump were much higher in case II than in case I. This is due to the larger horizontal temperature gradients that are maintained when heat escapes through the side walls (see Figure S9B). From previous studies of similar enzyme pumps,[*S4*] we know that the horizontal fluid flow speed (at locations far from vertical walls) is approximately proportional to the horizontal gradient in fluid density.

The flow speeds in case III were much lower than in cases I and II. The maximum flow speed per unit power was $u_{\max} \approx 10^{-4}\ \mu\mathrm{m\,s^{-1}}\ \mu\mathrm{W}^{-1}$, again occurring at the perimeter of the pump $(x = 3\,\mathrm{mm})$. Compared with cases I and II, the flow speed was more sharply peaked, decaying to 1% of the maximum value within a distance of about 2 mm on either side of the peak. This localized flow is consistent with simulation results reported by Sengupta et al.,[S6] who considered boundary conditions corresponding to case III (no heat flux through bottom and fixed temperature on top). Due to the shallow vertical dimension of the chamber, heat escapes rapidly from the system through the top boundary and is unable to spread far horizontally. The temperature rise is therefore much smaller than in cases I and II; density driven flows are correspondingly much slower.

Supplementary Calculations

To determine the maximum rate of heat production on the Au surface, the following calculations were done using the parameters in Table S1.

Table S1. Listed are different reactants for phosphatase and a comparison of selected parameters.[S7,S8]

Acid Phosphatase Reactants	Enthalpy (kJ/mol)	V_{max} (μmol min^{-1} mg^{-1})	K_M (mM)	Reaction Rate (mol/s)
5'-Adenosine Triphosphate	-107.9	329	0.054	2.6×10^{-10}
p-Nitrophenyl Phosphate	-25.9	605	0.091	4.7×10^{-10}
Pyrophosphate	-15.5	463	0.027	3.6×10^{-10}
α-Naphthyl Phosphate	-6.5	325	0.29	2.5×10^{-10}
5' Adenosine Monophosphate	-6.5	49	4.1	3.8×10^{-11}

Heat Production in Acid Phosphatase Pumps

Dimensions of micropumps:

Radius of Au patch: 3×10^{-3} m

Area of Au patch: 2.83×10^{-5} m^2

Height of chamber: 0.9 mm

Diameter of chamber: 20 mm

For Acid Phosphatase (radius = 4.7 nm) with ATP as the reactant:[S9]

Cross sectional area of a single enzyme molecule = $\pi \times (4.7)^2 \text{ nm}^2 = 69.4 \text{ nm}^2$

Area of the gold pattern = $\pi \times (3)^2 \text{ nm}^2 = 2.83 \times 10^{13} \text{ nm}^2$

Therefore, approximate number of enzyme molecule in the gold pattern:

$$= \frac{2.83\times10^{13}\ \text{nm}^2}{69.4\ \text{nm}^2} = 4.1\times10^{11}\ \text{molecules}\ = 6.77\times10^{-13}\ \text{mol}$$

We need to determine the reaction rate or V:

$$\text{V} = \frac{\text{V}_{\text{max}}\left[\text{S}\right]}{\text{K}_{\text{M}} + \left[\text{S}\right]} = \text{V} = \frac{329\ \mu\text{mol}\cdot\text{min}^{-1}\cdot\text{mg}^{-1}\left[50\ \text{mM}\right]}{0.054\ \text{mM} + \left[50\ \text{mM}\right]} \sim 329\ \mu\text{mol}\cdot\text{min}^{-1}\cdot\text{mg}^{-1}$$

The reaction rate value is given in $\mu\text{mol}\cdot\text{min}^{-1}\cdot\text{mg}^{-1}$ units. Multiplying the amount of enzyme (in mg) with the reaction rate value for ATP (329 $\mu\text{mol}\cdot\text{min}^{-1}\cdot\text{mg}^{-1}$) results in the desired units needed to calculate the heat production.[S8]

Molecular weight of 69 kDa[S10] = 69,000 g/mol. Thus, the amount of enzyme on the gold pattern:

$$= 6.77\times10^{-13}\ \text{mol}\ \times\ 6.9\times10^{7}\ \text{mg/mol} = 4.7\times10^{-5}\ \text{mg}$$

Thus, the reaction rate is:

$$= 329\ \mu\text{mol}\cdot\text{min}^{-1}\cdot\text{mg}^{-1}\ \times\ 4.7\times10^{-5}\ \text{mg}\ = 1.5\times10^{-2}\ \mu\text{mol}\cdot\text{min}^{-1}\ \times\ \frac{\text{mol}}{10^{6}\ \mu\text{mol}}\ \times\ \frac{\text{min}}{60\ \text{s}}$$

$$= 2.6\times10^{-10}\ \text{mol/s}$$

The amount of heat generated in the system:[12]

$$= 2.6\times10^{-10}\ \text{mol/s}\ \times\ \Delta H_{\text{Acid Phosphatase}} = 2.6\times10^{-10}\ \text{mol/s}\ \times\ 107.9\ \text{kJ/mol} = 2.8\times10^{-5}\ \text{J/s}$$

References:

S1. Özişik, M. N. *Finite Difference Methods in Heat Transfer.* CRC Press: Boca Raton, **1994**.

S2. Qian, Y. H.; Orszag, S. A. Lattice BGK Models for the Navier-Stokes Equation: Nonlinear Deviation in Compressible Regimes. *EPL* **1993**, *21*, 255.

S3. Aidun, C. K.; Clausen, J. R. Lattice-Boltzmann Method for Complex Flows. *Annual Review of Fluid Mechanics* **2010**, *42*, 439–472.

S4. Ortiz-Rivera, I.; Shum, H.; Agrawal, A.; Sen, A.; Balazs, A. C. Convective Flow Reversal in Self-Powered Enzyme Micropumps. *PNAS* **2016**, *113*, 2585–2590.

S5. Mezrhab, A.; Bouzidi, M.; Lallemand, P. Hybrid Lattice-Boltzmann Finite-Difference Simulation of Convective Flows. *Computers & Fluids* **2004**, *33*, 623–641.

S6. Sengupta, S.; Patra, D.; Ortiz-Rivera, I.; Agrawal, A.; Shklyaev, S.; Dey, K. K.; Córdova-Figueroa, U.; Mallouk, T. E.; Sen, A. Self-Powered Enzyme Micropumps. *Nat Chem* **2014**, *6*, 415–422.

S7. Goldberg, R. N.; Tewari, Y. B. Thermodynamics of Enzyme ‐ Catalyzed Reactions. Part 3. Hydrolases. *J. Phys. Chem. Ref. Data.* **1994**, *23*, 1035–1103.

S8. Van Etten, R. L.; Waymack, P. P. Substrate Specificity and pH Dependence of Homogeneous Wheat Germ Acid Phosphatase. *Arch. Biochem. Biophys.* **1991**, *288*, 634–645.

S9. Ostrowski, W.; Wasyl, Z. Stoke's Radius and Frictional Ratio of Human Prostatic Acid Phosphatase. *Biochim. Biophys. Acta* **1969**, *181*, 479–482.

S10. Kruzel, M.; Morawiecka, B. Acid Phosphatase of Potato Tubers (Solanum Tuberosum L). Purification, Properties, Sugar and Amino Acid Composition. *Acta Biochim. Pol.* **1982**, *29*, 321–330.